AIAA SciTech Forum
8-12 January 2024, Orlando, FL
AIAA SCITECH 2024 Forum

10.2514/6.2024-1135

Carbon Transport in Electric Propulsion Testing – I: Multiscale Computations for Carbon Sputtering by Low Energy Ion Bombardment

H. Tran[1], S. Clark[1], R. Thompson[1], DA. Levin[2], J. Rovey[2], H.B. Chew[3]
University of Illinois at Urbana Champaign, Talbot Laboratory, 104 S. Wright St, Urbana, Il, USA, 61801

A quantitative assessment of carbon transport during ground-based testing of high-power electric propulsion (EP) thrusters is essential for accurate lifetime assessment. Novel experimental carbon tracking techniques based on isotopic labeling of ^{13}C, in concert with Direct Simulation Monte Carlo (DSMC) plasma simulation techniques, have added the capability to elucidate the effects of carbon contamination on critical EP surfaces. Here, a multiscale sputtering simulation framework is used to inform and validate these carbon transport experimental-simulation models. Specifically, molecular dynamics (MD) simulations, upscaled to Monte Carlo (MC) simulations are adopted to quantify the relevant macroscopic sputtering properties (sputter yield, angle, and energy) of carbon under krypton ion bombardment at 300 eV. The multiscale sputtering simulation is able to capture the smoothening behavior observed from post-sputtered surface analysis of a ^{13}C pellet from a hall thruster. The sputtering properties from our MD-MC models will be used to inform the boundary conditions of the DSMC-based carbon transport model.

I. Introduction

The need for an efficient, high-thrust space propulsion system to augment or replace traditional chemical propulsion systems is of great national importance, and is paramount to advancing space technology in the United States. Even though Spacecraft Electric Propulsion (EP) has been an integral part of space exploration since the late 1950s, high-power EP (>100 kW) remains largely an engineering concept due to insufficient correlation between ground-test experimental results versus in-space performance and wear. Specifically, ground-based EP test measurements cannot adequately represent in-space environment, due to facility effects interacting with thruster operations [1]. One major challenge is the presence of contaminants from the facility walls interacting with the ion thruster through back sputtering, contaminant transport, and redeposition. To reduce these facility back-sputtering effects, the walls of the testing chamber are typically lined with "sputter-resistant" graphitic panels. Nevertheless, at high ion energies, even pyrolytic graphite can undergo significant sputtering, resulting in the dispersion and transport of these back-sputtered carbon species throughout the facility [2,3]. Since the EP's thruster life-limiter ties directly to the erosion rate of critical thruster's components, including the carbon pole covers, center-mounted cathode, anode, molybdenum's ion engine grid, and boron nitride channels, the subsequent deposition of back-sputtered carbon species on these critical components lead to significant uncertainties in EP thrusters' lifetime and performance assessments. Currently, quantifying such carbon contamination effects experimentally is highly nontrivial and is an ongoing research challenge.

On the simulation side, Particle-In-Cell (PIC) or Direct Simulation Monte Carlo (DSMC) models such as CHAOS, simulate the plasma environment and can be used to elucidate the effects of carbon deposition on critical EP surfaces [4,5]. CHAOS simulation results on the effect of backsputtering suggest that the carbon deposition rate on the thruster is significantly influenced by the angular dependence of the sputtered carbon, with a nearly 50% effect [6].

[1] Ph.D. Candidate, Aerospace Engineering Department
[2] Professor, Aerospace Engineering Department
[3] Associate Professor, Aerospace Engineering Department

Experimentally, one method to differentiate between facility and thruster sourced carbon is to use isotopically labeled carbon ^{13}C materials. By replacing the graphite pole covers with a high purity ^{13}C pole cover, conductive carbon film deposition collected on substrates placed along the channel walls can be differentiated from deposition of backsputtered facility ^{12}C carbon. Further, the isotopically labeled materials can be used as sputtering targets in the plumes of thrusters. To demonstrate the capabilities of the ^{13}C isotopic tracking as a diagnostic method while providing experimentals inputs to tune PIC-DSMC carbon transport plasma models, we conduct a four hour long test, subjecting two ^{13}C pellets to low energy krypton ion bombardment. We collect the ^{13}C sputterants from the pellets and the ^{12}C sputtered from the beam dump through various substrates with different materials and roughness.

Both the experimental setup and the carbon transport model require detailed information on the sputtering yield of a given graphitic structure as a function of the incident ion type (Xe, Ar, Kr), energy, and angle, as well as surface morphology [7]. The experimental setup was guided by differential and total sputter yield data to determine the placement of substrates and time required for sufficient deposition of ^{13}C sputterates for isotopic concentration diagnostics. In addition, material sputtering data would serve as a boundary condition for the simulation domain of CHAOS or any plasma simulation code in general. The non-linear parametric dependence can be quite complex, and contributes to a range of direct, binary, or collision cascade mechanisms that can influence the overall sputtering rate [8]. Semi-analytical theories have been proposed by Yamamura and others to estimate sputter yields for various ion-elemental targets (typically metallic alloys). However, these analytical formulations tend to underpredict experimental sputter yield [9,10], especially under the low ion energies (100-1000 eV) since these semi-empirical models cannot adequately capture the sputtering rates in covalently-bonded structures such as ceramics materials which undergo amorphization under ion bombardment. Furthermore, other simulations method such as Transport of Ions in Matter (TRIM) or the Stopping Range of Ions in Matter (SRIM), are based on binary collision approximation (BCA), which breaks down at these low ion energies due to its inability to handle many-body interactions [11].

In this work, we perform the analysis on the sputtering characteristics of ^{13}C pellet as the first step in understanding carbon transport in ground-based testing of EP thrusters detailed in Section II. We describe the multiscale sputtering simulation approach [12,13] in Section III. We apply this simulation framework to elucidate the sputtering properties of our ^{13}C pellet and validate our simulation predictions with the ground-based sputtering experiments in Section IV. We discuss the next step of our efforts and conclude with a summary in Section V.

II. ^{13}C Isotopic Tracking Diagnostic Method Validation Experiment

The experimental setup (Fig. 1) consisted of two labeled ^{13}C pellets placed one meter downstream of the exit plane and aligned to the channel center of a 4.5kW HET operating at 300V on krypton. The first pellet is secured in an alumina tube and wired to a power supply, acting as a Faraday probe to measure the current density. The pellet is biased from 0 to -30 V in 5 V increments at the onset and just before the conclusion of ion bombardment to repel electron bombardment that would detract from ion current measurement. Two rows of substrates are placed with the geometry to collect ^{13}C deposition from the pellet and ^{12}C backsputtered from the beam dump (Fig. 1b and 1c). The substrates systems consist of different materials and different surface roughness (Fig. 1c), providing ^{13}C differential sputtering information along with ^{13}C deposition characteristics at various ^{13}C incidence angles and substrate material properties.

A second (controlled ^{13}C) pellet is placed inside of a closed environment (Fig. 1d), consisting of a triple collimated structure wrapped in Nickle shim. The leading ceramic plate has an 8mm aperature and the back two aluminum plates, each with 6mm apertures. This second pellet are shielded from deposition of backsputtered facility ^{12}C. A known ^{13}C concentration pellet provide a thin film with the same isotopic content as the bulk material. The facility contribution to deposition is obtained from a quartz crystal microbalance (qcm) placed in the exit plane of the thruster. Based on Faraday probe measuerments, it is estimated that the primary (open environment) pellet was bombarded by 9×10^{19} ions/cm^2/hour, while the closed environment pellet is exposed to 6×10^{19} ions/cm^2/hour. The whole experiment, except for the two sputtered ^{13}C pellets, is shielded thermally through a graphitic panel (Fig. 1b).

To synthesize the labeled ^{13}C pellets, 99% amorphous ^{13}C powder (Cambridge Isotopes) is used. A binding agent, comprised of 50 wt% poly(furfuyl) alcohol (Polysciences), 48 wt% acetone, and 2 wt% Maleic Anhydride (Millipore Sigma), is added to the powder at 5 wt%. The slurry is mixed in a centrifugal mixer at 1400 RPM. The acetone is allowed to evaporate at room temperature and the mixture is placed into a 1 cm die and compressed at 30 MPa in a hydraulic pellet press. Further densification is done in a cold isostatic press at 215 MPa. The pellets are then cured at

can be

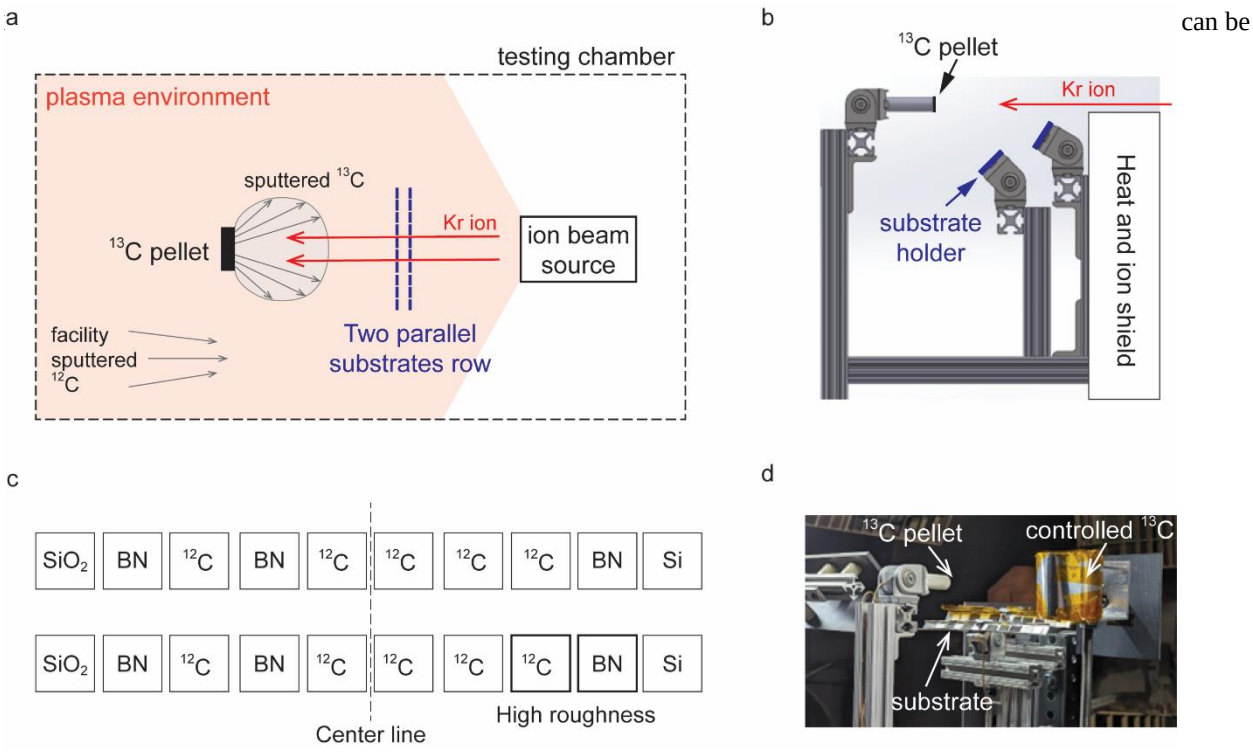

Fig. 1: (a,b) Schematic of the experiment setup (a), along with side view of the first ^{13}C pellet (b) showing the relative placement of the pellet, the substrate holder and the shield with respect to the krypton ion incidence angle. (c) Collection substrate configurations and materials, located in 'blue' plate in (b). (d) Experimental setup inside the testing chamber, depicting both the sputter-deposited ^{13}C pellet and the controlled ^{13}C pellet.

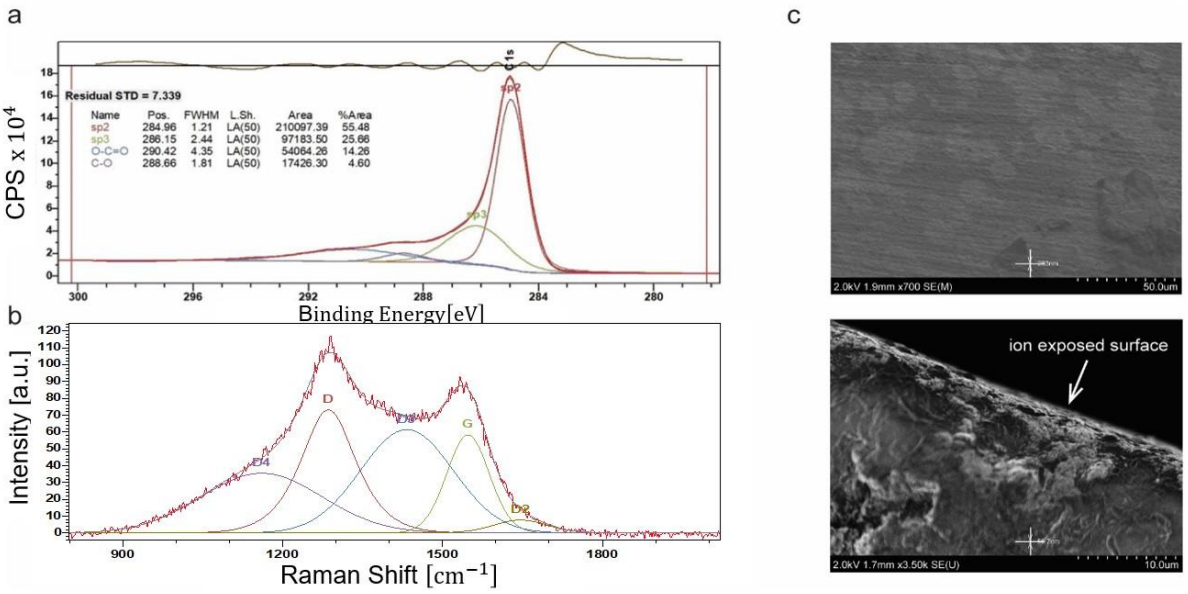

Fig. 2: Material analysis of the ^{13}C pellet prior to performing the sputtering experiments. (a) Deconvolved XPS spectra of ^{13}C pellet showing hybridization ratios. (b) Raman spectra of the amorphous ^{13}C pellet with deconvolved sp^2 (G-peak) vibrational modes red-shifted due to the increased mass of ^{13}C. (c) SEM images of the contained carbon ^{13}C pellet showing uniformity of the surface roughness.

found in previous work [14]. The isotopic concentration of the pellets is analyzed through isotope ratio mass spectrometry and time-of-flight secondary ion mass spectrometry. The $^{13}C/^{12}C$ measurements of the two techniques agree well and the pellets are found to have a mass concentration of 94% $^{13}C/C$.

The surface topology of the pellets is analyzed both pre- and post-bombardment through 10× (90 nm resolution) and 150× (0.9 μm resolution) lenses with a Keyence VK-X1000 3D Laser Scanning Confocal Microscope and complimented with Secondary Electron Microscopy images. To monitor the evolution in bond structure during irradiation, XPS and Raman spectra are taken both prior to and after irradiation. Along with the current density measurements, a mass balance with 10µg precision is used to collect mass loss measurements for total sputter yields. Before mass measurements, the pellets are placed in a furnace at 80℃ for 24hrs and transferred to the mass balance, which is located within a humidity-controlled environment. Fig. 2 shows the preliminary analysis of the pellet prior to the ion bombardment. XPS results (Fig. 2a) suggests the pellet consists of 55% sp^2 bond with 25% sp^3 bond, represents clearly in the distinct G and D peak from Raman analysis (Fig. 2b). Additionally, the pellet is also sanded to achieve a uniformity roughness to minimize experimental uncertainty (SEM images in Fig. 2c).

III. Carbon Sputtering Scale-Bridging Modeling

The goal of this experiment is to delineate the amount of ^{13}C from the pellet and ^{12}C from the facility backsputtered at the collector substrate. Here, we employ a multiscale modeling approach to predict the sputtering characteristics (yield and differential profile) of the ^{13}C pellet, which will help inform the experiment setup and testing time to achieve a sufficiently thick deposited carbon film (of at least 10 nm) in the substrate for XPS and Raman spectra measurements.

As detailed in our recent papers [12,13], the framework employs molecular dynamics (MD) simulations with well-calibrated interatomic potentials to elucidate the sputtering mechanisms, as well as to quantify the parametric effects of ion incidence angle and incidence ion energy distributions on the sputtering rate. Because MD simulations are computationally expensive, and are typically limited to length-scales of several tens of nanometers, we subsequently employ kinetic Monte Carlo (MC) to simulate surface morphology evolution and its effect on the macroscale sputtering properties, with the elemental sputtering properties of the MC model (e.g., sputtered velocity and angle distribution, ion absorption rate, and sputtered yield) computed from MD simulations.

A. Molecular Dynamics Modeling

Our MD simulations are performed using the classical MD simulator, LAMMPS. The interatomic interactions potential between the carbon atoms are governed by an Adaptive Intermolecular Reactive Empirical Bond Order (AIREBO) potential that has been widely verified with quantum calculations and experiments [15]. Due to the non-reactive nature of inert gas, its interactions with the carbon substrate is governed by the classical Ziegler-Biersack-Littmark (ZBL) potential [16]. This ZBL potential can only account for screened nuclear repulsion associated with high-energy collision between atoms and is deemed suitable when the nucleus interaction trumps over electron cloud interactions, which is expected at ion energies of 25 to 1000 eV. For instance, using Density Functional Theory (DFT) calculations with VASP [17], we have performed a series of validation studies demonstrating that this simple ZBL potential accurately captures the repulsive interaction and cut-off radius between Carbon and inert gas pair atom interactions (such as Xenon or Krypton) across various s, sp, and sp^2 configurations of carbon.

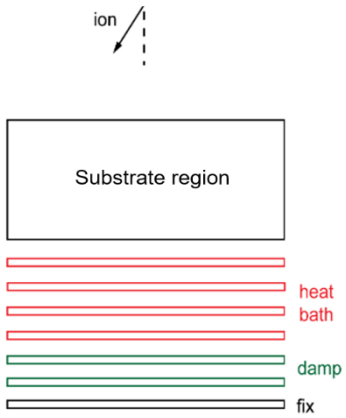

Fig. 3: Schematic of the MD simulation set up for the time-accelerated sputtering simulation.

In our MD simulations, we employ a time-accelerated sputtering simulations that has been widely adopted to study the sputtering mechanisms of various material structures (Fig. 3) [18,19]. Particularly, prior to initiating the bombardment sequence, we subject the substrate material (for example, multilayer graphene with ABA stacking normal orientation for pyrolytic graphite material) to an NVT ensemble

maintained at a desirable temperature by a Berendsen thermostat. For each simulation step, we deposit one inert gas ion (Xe, Ar, Kr) randomly above the substrate's surface with a time step of 0.1 fs; each ion has initial velocity in the -z, +x, +y direction corresponding to the kinetic energy of 25 – 1000 eV and an incidence angle of between 0° and 75°. After initiating this deposition process, we equilibrate the entire system without a thermostat for the first 1 ps to resolve the initial impact dynamics. Thereafter, we switch on the thermostat in the heat-bath region and set it to the target temperature for the next 20 ps, before quenching the surface layer to that temperature for a further 20 ps. The equilibration and the quenching process have time step of 1 fs. After each bombardment cycle, we capture the species that escape the simulation box, noting the species type, energy, and trajectory. The entire bombardment sequence is then repeated to characterize the elemental sputter yield of a given inert gas – material system.

B. Kinetic Monte Carlo Modeling

The initial carbon surface of arbitrary morphology is discretized into one-dimensional, two node elements, each of fixed horizontal dimension, dx (refer to [13] for details of the simulation setup). The simulation box is periodic in the x-direction with box length λ. For each ion bombardment process, a random inert gas atom is deposited randomly above the substrate surface with an initial incidence kinetic energy, E_{Kr}, and angle, θ_{Kr}. Upon impact of the atom on the surface, the sputter yield, which is a known function of the xenon ion incidence energy and local incidence angle from MD, is used to compute the probability of carbon sputtering. These sputtered atoms have energies E_C and trajectories θ_C that are statistically selected based on the cumulative distribution functions $(g(E_C), f(\alpha_C))$, obtained from MD for a given (E_{Kr}, θ_{Kr}). Subsequently, the sputtered carbon atom either impacts another surface or escapes from the simulation box to yield a sputterant. In the case of the former, the probability of emission of a secondary sputtered atom is computed based on its energy E_C and local incidence angle θ_C, once again, obtained from MD simulations. The trajectory of this secondary sputtered atom follows a cosine distribution [20]. Should the secondary atom impact an additional surface, we assume that the atom will be deposited on the surface with 100% probability. We trace the evolution of the morphology by changing the height $h(x)$ of the respective nodes when carbon atoms leave or are redeposited onto the surface. In this MC algorithm, the effects of surface diffusion are deemed to be negligible in view of the covalently bonded structure of ceramics characterized by high bond strength.

IV. Results

We first conduct the MD simulations on krypton bombardment onto multi-layer graphene (pyrolytic graphite) at krypton incident energy $\boldsymbol{E_{Kr} = 300\ eV}$ to mimic the experiment conditions described in section 2. The simulation shows that the initial penetration of krypton ions within the graphite layers at high velocities causes significant disruption to the atomic arrangement of carbon atoms (Fig. 4a-c). Further carbon-carbon bond breaking and bond rearrangements are observed with repeated ion bombardment (increasing fluence), resulting in amorphization of the graphitic subsurface spanning the average penetration depth of the krypton ion. To quantify the structural characteristics of this amorphized carbon layer, we average the percentage of sp and sp^2 bonds, as well as the atomic density, within the volume of the amorphized region. Figure 4d and 4e shows the evolution of the relative bond fraction and porosity of the amorphous carbon at three different incidence krypton angle $\theta_{Kr} = 0°, 30°, 60°$. Regardless of the krypton ion incidence angle, the percentage of sp^2 bonds decreases with Kr fluence while the percentage of sp bonds correspondingly increases (Fig. 4d). Similarly, the structure becomes more porous with bombardment, as shown by the decrease in the atomic density (Fig. 4e). Beyond a certain fluence, the structural characteristics of this amorphous subsurface remain unchanged, representing by the plateau of the bond ratio and the atomic density. More interestingly, these plateau values are nearly identical regardless of the krypton incidence angle, suggesting that the amorphous carbon structures at steady state are independent from the krypton incidence angle.

We show the relationship between the sputter yield as a function of the incidence krypton angle θ_{Kr} in Fig. 4f. The maximum sputter yield is obtained at $\theta_{Kr} = 75°$, which is almost two-order of magnitude higher than the sputteryield at normal incidence angle. Another information that is required for MC model are the probability distribution function (PDF) of the carbon sputter angle θ_C and carbon sputter energy E_c. From MD simulations, we can trace the energy and the local angle emission of the carbon sputterants, ranging from $-90°$ to $90°$ with respect to the surface normal under steady-state bombardment and construct the appropriate distribution profile. Fig. 5 plots the obtained PDF of sputter carbon angle, θ_C, and sputter carbon energy E_C, across different incidence krypton angle θ_{Kr}.

At low $\theta_{Kr} \leq 30°$, the PDF of the sputter angle is relatively symmetrical and follows the typical cosine distribution proposed by Sigmund [20]. However, at high oblique incidence angle, the differential yield profile becomes more skewed, and favors the forward scatter direction ($\theta_C > 0°$) (Fig. 5a). The emitted carbon sputterants have energies of ~1.5 eV, except for $\theta_{Kr} = 75°$ where higher energies of ~10 eV are observed (Fig. 5b).

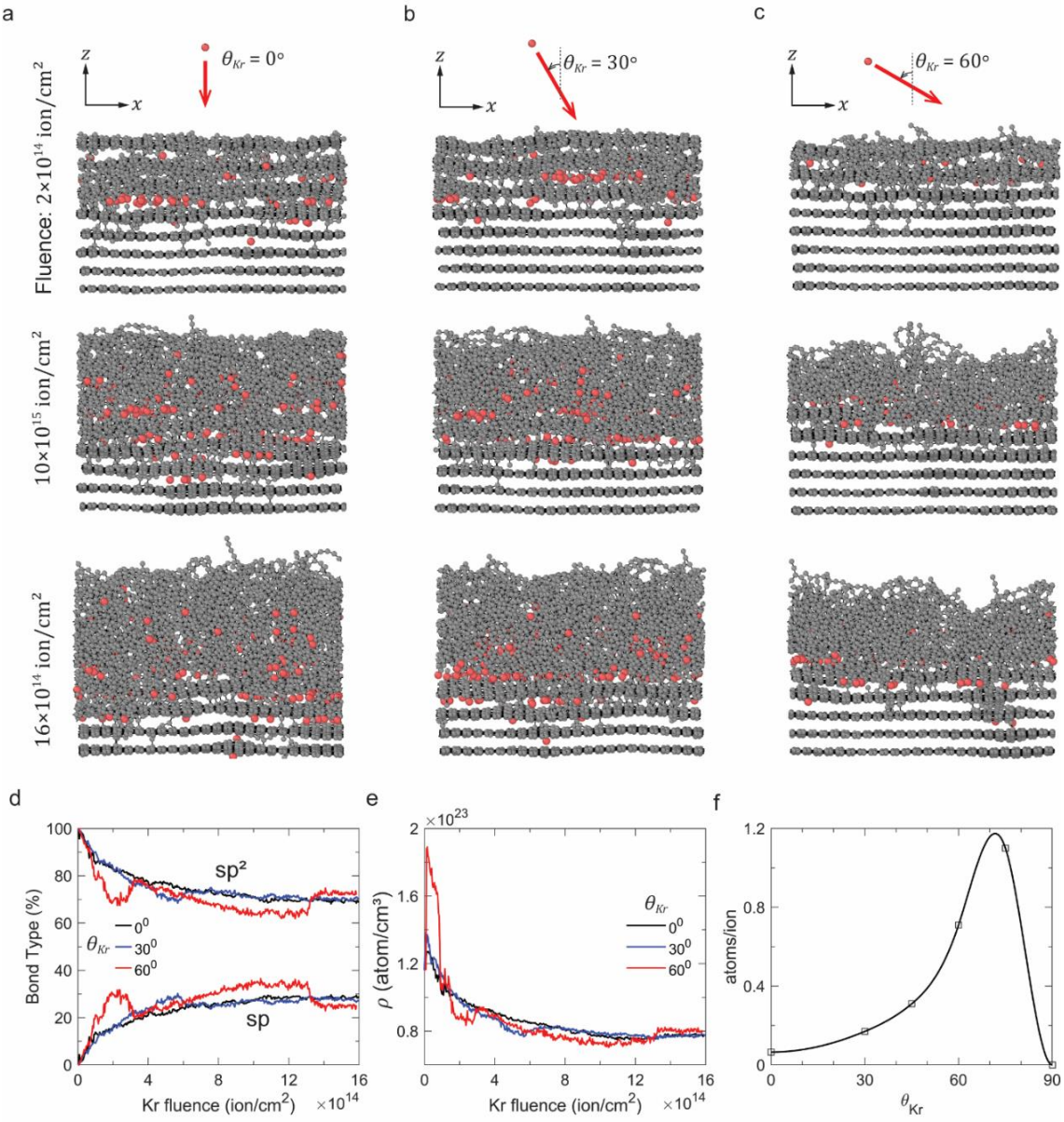

Fig. 4: (a,b,c) Evolution of the atomistic configurations of a graphitic substrate with ion fluence under $E_{Kr} = 300\ eV$ at Kr incidence angle $\theta_{Kr} = 0°$ (a), $\theta_{Kr} = 30°$ (b), $\theta_{Kr} = 60°$ (c). (d,e) Evolution of the proportion of sp and sp² bonds (d) and atomic density (e) within the amorphous subsurface for $\theta_{Kr} = 0°$ (black), $\theta_{Kr} = 30°$ (blue), and $\theta_{Kr} = 60°$ (red). (e) Sputter yield as a function of incidence Krypton ion θ_{Kr} for $E_{Kr} = 300$ eV; symbols denote the steady-state sputtering yield, obtained from MD simulations connected with a spline fitting, with exception for $\theta_{Kr} = 90°$ where the yield of 0 (atoms/ion) is assumed.

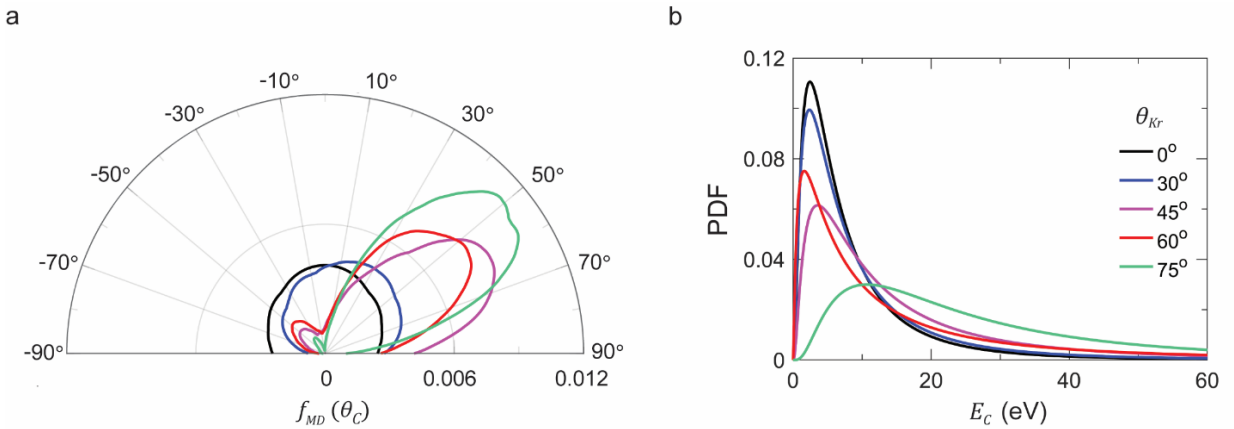

Fig. 5: Probability Distribution Function (PDF) of sputter carbon angle, θ_C (a), and sputter carbon energy E_C, (b) obtained from MD simulations across different incidence krypton angle θ_{Kr} and at $E_{Kr} = 300\ eV$.

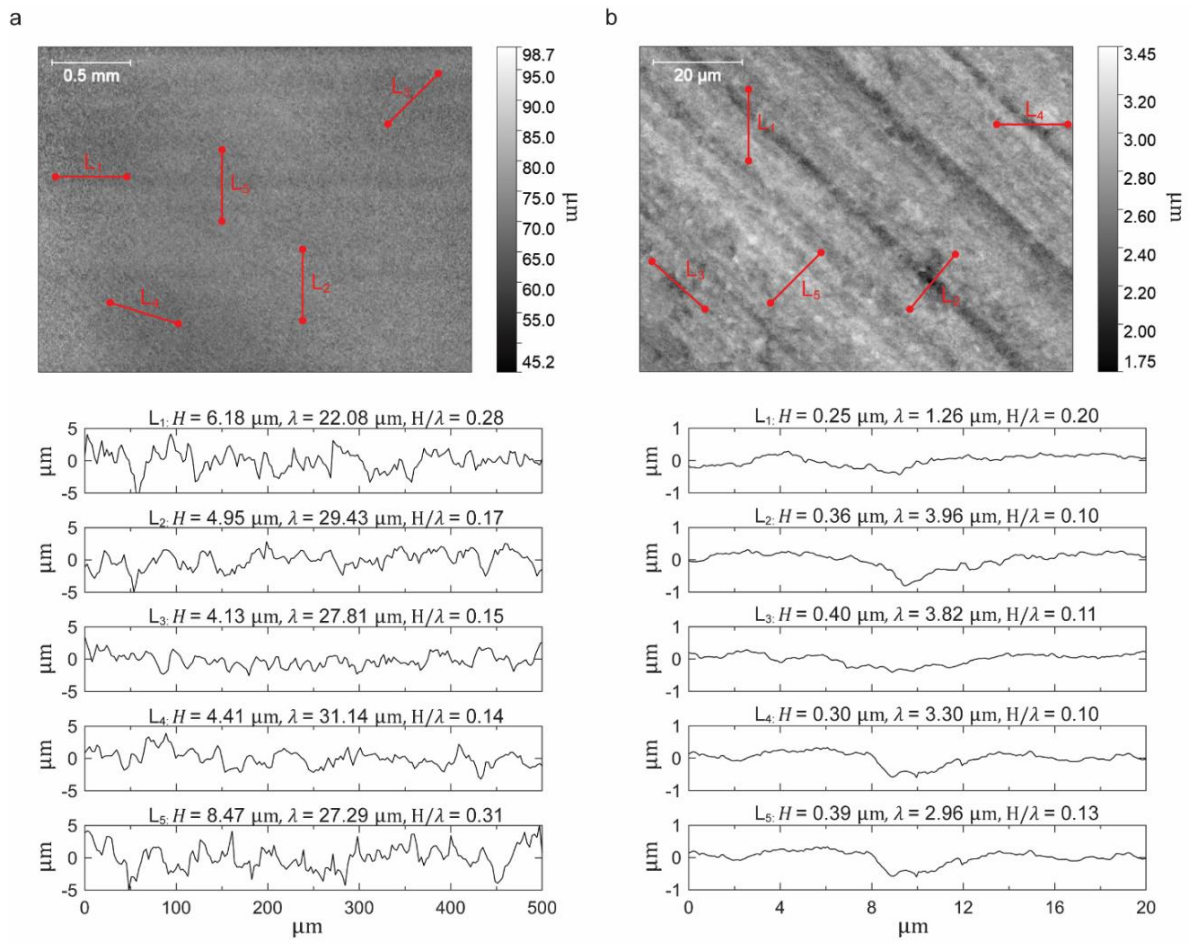

Fig. 6: Profilometry, conducting using the Keyence VK-X1000 3D Laser Scanning Confocal Microscope, of the ^{13}C carbon pellet (Fig. 1) before sputtering by krypton bombardment at two distinctive length scales (a,b). Top view: overall image. Bottom view: detailed one-dimensional surface plot of lines L_1 to L_5 (red) in overall image. The roughness height, H, and the average wavelength, λ, is estimated following ASME B46.11998 and ISO 4287-1997 standards with the high-frequency components [21] that best represent the domain of the Monte Carlo simulation.

MD simulations show that the initial surface morphology has pronounced effects on the sputter yield and the required fluence to attain the steady-state under low xenon ion energy bombardment of carbon substrates [12,13]. Given that xenon and krypton are both significantly heavier (in terms of atomic number and atomic mass) than carbon, we similarly expected the strong dependence of the sputter yield evolution on surface morphology under Kr ion bombardment. We measure the initial surface morphology of the ^{13}C pellet through Laser Scanning Confocal Microscope at two distinct length scales prior to performing the sputtering experiment (Fig. 6), and show that the initial surface is smooth with maximum variation of $\pm\ 50\mu m$ within 2.5 mm^2 area (Fig. 6a-top) and $\pm 0.85\ \mu m$ within 0.1 mm^2 area (Fig. 6b-top). For each image, we show line scans L_1 to L_5 of the detailed surface texture. The one-dimensional texture (Fig. 6a,b bottom) is decomposed into waviness (the low-frequency components defining the overall shape) and roughness (the high-frequency components) at the cut-off frequency. This frequency is specified in units of the Nyquist frequency. For MC modeling, we are interested in the roughness (high frequency components) of the surface profile with the local roughness r_j at the surface point j where the mean value of r_j is zero across the one-dimensional surface texture. Following ASME B46.1-1995 and ISO 4287-1997 standard [21], for the given average high frequency, $\boldsymbol{\lambda}$, obtained from frequency domain decomposition method [22], we define the mean peak-to-valley height of the profile as:

$$\boldsymbol{H} = R_{vm} + R_{pm}$$

where R_{vm} is the mean valley depth based on one peak per sampling length:

$$R_{vm} = \frac{1}{m}\sum_{i=1}^{N} |\min\ r_j| \text{ for } \frac{(i-1)N}{m} < j < \frac{iN}{m},$$

and R_{pm} is the mean peak height based on one peak per sampling length:

$$R_{pm} = \frac{1}{m}\sum_{i=1}^{N} |\max\ r_j| \text{ for } \frac{(i-1)N}{m} < j < \frac{iN}{m}$$

We choose $m = 5$ for our analysis and denote the calculated H, λ values for each line scan L_1 to L_5 in Fig. 6. The average roughness, $\frac{\boldsymbol{H}}{\boldsymbol{\lambda}}$, fluctuates between $0.14 - 0.31$ at the large length scale (Fig. 6a) and between $0.1 - 0.2$ at the smaller length scale (Fig. 6b). In our MC model, we represent this average $\frac{H}{\lambda}$ as an idealized periodic undulating sinusoidal topology along the x-direction:

$$h(x) = \frac{H}{2}\left(1 - \cos\left(\frac{2\pi x}{\lambda}\right)\right)$$

where $\frac{H}{2}$ denotes the amplitude of the surface roughness. We conduct MC simulations with three different initial surface morphologies, $\frac{H}{\lambda} = 0.1, 0.2$ and 0.3, and show in Fig. 7a the evolving surface configurations 0-3 under a

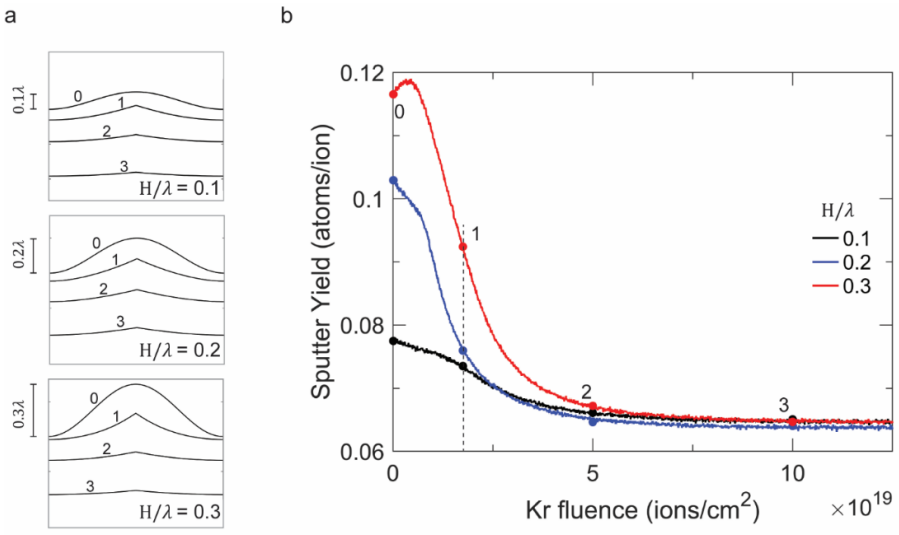

Fig. 7: (a) Snapshots of the evolving surface morphologies under $E_{Kr} = 300$ eV and $\theta_{Kr} = 0°$ at three different initial roughness ($\frac{H}{\lambda} = 0.1, 0.2, 0.3$ from top to bottom). (b) Evolution of the sputtering yield for each initial roughness in (a). The numbers 0-3 in (a) denote the corresponding fluences depicted in (b).

normal Kr ion incidence. Regardless of the initial surface roughness, a microscopically flat surface is eventually obtained under steady-state sputtering (configuration 3). The morphology evolution under krypton ion fluence is accompanied by changes to the macroscopic sputtering yield as shown in Fig. 7b. While the initially rough surface topology has a high initial sputter yield, the sputtering yield for all three initial roughness configurations monotonically decreases with Kr fluence until steady-state sputter yield (corresponding to configuration 3) is achieved after Kr fluence of $7 \times 10^{19}\ ions/cm^2$.

We repeat the analysis with the initial roughness of $\frac{H}{\lambda} = 0.3$ but with different incidence Krypton angle, θ_{Kr} (Fig. 8). The sputtering process becomes more complicated under a oblique ion incidence, triggering multiple erosion and deposition mechanisms at multi-scales. This is in part because of the activation of surface shielding effects which are absent under a normal ion incidence. These effects result in the development of distinctive morphology changes at the microscale: an undulating and ever-changing morphology. However, these microscale undulations have a common characteristic: the ion- and back-facing sides are approximately normal and parallel to the incidence ion flux, resembling surface steps. The flattening of the ion-facing surface is similar to the morphology transition from a rough to a uniformly flat surface under a normal ion incidence. On the back-faces, any undulations are rapidly eroded by the ion flux to create a flat, parallel surface that is shielded from the incidence ions (Fig. 8a). These ever-changing, yet self-similar surface steps result in a fluctuating sputter yield, albeit about a steady-state mean value (Fig. 8b). Since the sputter angle PDF is strongly dependent on the instantaneous surface profile, we average the sputter angle response after 5×10^{19} $(ions/cm^2)$ to construct the PDF profile (Fig. 8c).

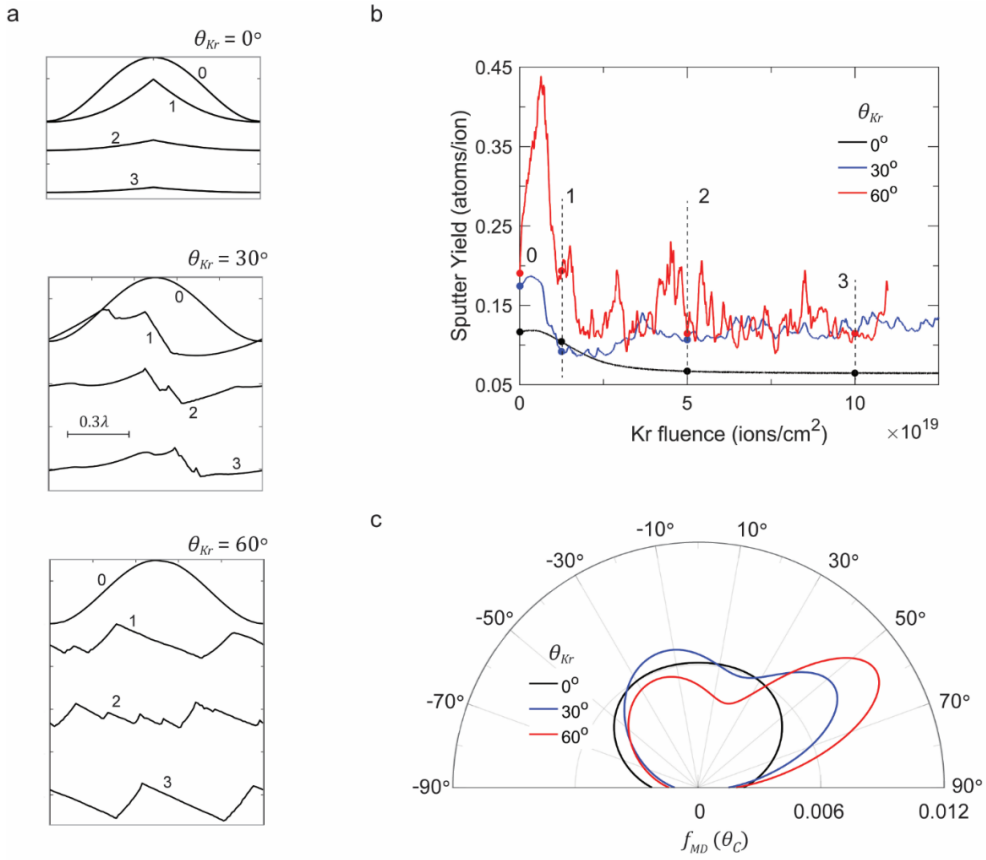

Fig. 8: (a) Snapshots of the evolving surface morphologies under $E_{Kr} = 300$ eV for initial surface roughness, $\frac{H}{\lambda} = 0.3$ at three different $\theta_{Kr} = 0°, 30°, 60°$ (from top to bottom). (b) Evolution of the sputtering yield for each θ_{Kr} in (a). The numbers 0-3 in (a) denote the corresponding fluences in (b). (c) Probability Distribution Function (PDF) of the angle of the carbon sputterants, θ_C, at steady-state.

V. Discussions and Conclusions

The surface morphology of the ^{13}C carbon pallet is re-analyzed after the sputtering experiments have been performed for one hour under a normal krypton ion incidence. Fig. 9 shows the surface profile, conducting within 1 mm^2 area, after subjecting the 13C pellet to a corresponding fluence of 7×10^{19} (ions/cm^2). When comparing to the same length scale morphology from the pre-bombardment analysis (Fig. 6a), the surface variations reduce significantly to almost 50% ($\pm$ 50 μm to ± 30 μm). The detailed surface texture of five representative line L_1 to L_5 shows distinct smoothening where the average profile roughness, $\frac{H}{\lambda}$, are all less than 0.1, with the presence of the transition triangular shape morphologies (L_1). The post surface profile is in good agreement with the simulation observations (Fig. 7a). While we do not measure the steady-state sputtering yield directly from our experimentation, we note that the predicted steady-state sputtering yield from our simulations with krypton under a normal incidence angle is similar to prior experiments by Bohdansky (0.065 atoms/ion vs 0.084 atoms/ion) [23]. ***We remark that the results obtained from our multi-scale MD-MC simulations: (1) carbon amorphization, (2) carbon structure independence at steady state sputter yield, (3) surface smoothening at normal incidence angle, and (4) characteristic surface steps at oblique incidence angle for krypton is similar to what has been observed under xenon ion bombardment of carbon materials [12,13,24,25]***

As previously mentioned, the goal of this multi-scale materials modeling is to provide an accurate carbon sputtering response (sputter yield, angle PDF, energy PDF) to be implemented as boundary conditions for the CHAOS carbon transport code, as well as to inform experiments. For ease of implementation, we describe the PDF of the sputter carbon angle as a linear combination of two Gaussian function distributions, each representing the dominant forward ($0° < \theta_C < 90°$) and backward ($-90° < \theta_C < 0°$) scatter directions.

$$f(\theta_C) = \frac{A}{\sigma_1\sqrt{2\pi}} e^{-\frac{1}{2}\left(\frac{\theta_C-\mu_1}{\sigma_1}\right)^2} + \frac{1-A}{\sigma_2\sqrt{2\pi}} e^{-\frac{1}{2}\left(\frac{\theta_C-\mu_2}{\sigma_2}\right)^2}$$

where μ_j represents the peak sputtered angle, σ_j represents the spread due to the inelastic collisions, and A is the relative contribution of the forward ($j = 1$) and backward ($j = 2$)sputterants. Additionally, we describe the PDF of the sputter carbon energy as a log-normal functional form.

$$g(E_C) = \frac{1}{E_C\sigma_s\sqrt{2\pi}} e^{-\frac{1}{2}\left(\frac{\ln(E_C)-\mu_s}{\sigma_s}\right)^2}$$

The μ and σ value on the two equations above are fitted to the MC simulation results, and are summarized in Table 1.

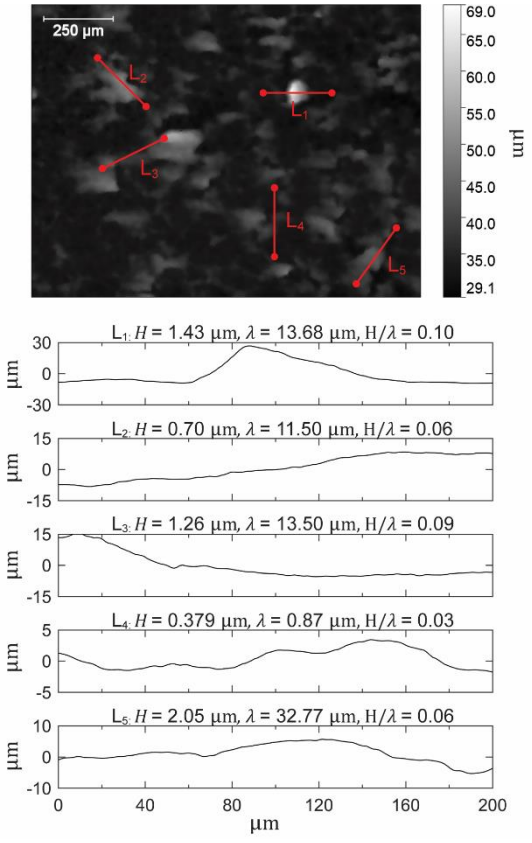

Fig. 9: Profilometry of the ^{13}C carbon pellet after subjecting to 7×10^{19} ions/cm^2 of krypton bombardment. The estimate roughness height, H, and the average wavelength, λ, is conducted following ASME B46.11998 and ISO 4287-1997 standard with the high-frequency components [21]

Table 1: Fitting parameters for the sputtering properties (sputter yield, sputter angle PDF, and sputter energy PDF) at steady-state for carbon substrates under krypton ion bombardment at E_{Kr} = 300 eV for different krypton ion incidence angle, θ_{Kr}.

θ_{Kr}	Mean Sputter Yield (atoms/ion)	Fitting parameters for PDF of sputtered carbon						
		Angle					Energy	
		μ_1	σ_1	μ_2	σ_2	A	μ_S	σ_S
0°	0.065	39.62	38.75	-39.69	39.15	0.50	1.787	0.94
30°	0.119	59.97	19.42	-5.6	42.84	0.28	1.89	1.01
45°	0.131	56.11	18.52	-13.99	40.14	0.31	2.37	1.05
60°	0.124	57.82	17.39	-20.99	41.50	0.41	2.28	1.34
75°	0.287	46.88	20.83	-38.66	33.37	0.79	2.11	0.86

Acknowledgments

This work is supported by NASA through the Joint Advanced Propulsion Institute, a NASA Space Technology Research Institute, under grant number 80NSSC21K1118. We acknowledge the use of computational resources under the Delta research computing project, which is supported by the National Science Foundation (award OCI 2005572), and the State of Illinois. Delta is a joint effort of the University of Illinois at Urbana-Champaign and its National Center for Supercomputing Applications. The use of the Advanced Cyberinfrastructure Coordination Ecosystem: Services & Support (ACCESS), through allocations MAT210031 and MSS22006, is also gratefully acknowledged.

References

[1] Lobbia, R. B., Polk, J. E., Hofer, R. R., Chaplin, V. H., and Jorns, B., "Accelerating 23,000 Hours of Ground Test Backsputtered Carbon on a Magnetically Shielded Hall Thruster," *AIAA Propulsion and Energy 2019 Forum*, American Institute of Aeronautics and Astronautics, 2019. https://doi.org/10.2514/6.2019-3898

[2] Soulas, G. C., "The Impact of Back-Sputtered Carbon on the Accelerator Grid Wear Rates of the NEXT and NSTAR Ion Thrusters," presented at the International Electric Propulsion Conference, Washington, D.C., 2013.

[3] Polk, J., Duchemin, O., Ho, C., and Koel, B., "The Effect of Carbon Deposition on Accelerator Grid Wear Rates in Ion Engine Ground Testing," *undefined*, 2000. Retrieved 22 November 2021. https://www.semanticscholar.org/paper/The-effect-of-carbon-deposition-on-accelerator-grid-Polk-Duchemin/45361c0cee4d0013ecebdb16bc85d6dea8a66370

[4] Jambunathan, R., and Levin, D., "Kinetic Modeling of Plasma Plumes Using Multi-GPU Forest of Octree Approach IEPC-2017-67," 2017. Retrieved 31 May 2022. https://www.semanticscholar.org/paper/Kinetic-Modeling-of-Plasma-Plumes-using-Multi-GPU-Jambunathan-Levin/1ab544fee334ea67a187ae3a1a114e2507c85d57

[5] Jambunathan, R., and Levin, D. A., "CHAOS: An Octree-Based PIC-DSMC Code for Modeling of Electron Kinetic Properties in a Plasma Plume Using MPI-CUDA Parallelization," *Journal of Computational Physics*, Vol. 373, 2018, pp. 571–604. https://doi.org/10.1016/j.jcp.2018.07.005

[6] Nishii, K., and Levin, D. A., "Three-Dimensional Kinetic Simulations of Carbon Backsputtering in Vacuum Chambers from Ion Thruster Plumes," *Journal of Propulsion and Power*, Vol. 0, No. 0, pp. 1–15. https://doi.org/10.2514/1.B39194

[7] Jambunathan, R., and Levin, D. A., "Kinetic, 3-D, PIC-DSMC Simulations of Ion Thruster Plumes and the Backflow Region," *IEEE Transactions on Plasma Science*, Vol. 48, No. 6, 2020, pp. 2017–2034. https://doi.org/10.1109/TPS.2020.2988010

[8] Eckstein, W., and Preuss, R., "New Fit Formulae for the Sputtering Yield," *Journal of Nuclear Materials*, Vol. 320, No. 3, 2003, pp. 209–213. https://doi.org/10.1016/S0022-3115(03)00192-2

[9] Yamamura, Y., and Shindo, S., "An Empirical Formula for Angular Dependence of Sputtering Yields," *Radiation Effects*, Vol. 80, Nos. 1–2, 1984, pp. 57–72. https://doi.org/10.1080/00337578408222489

[10] Yamamura, Y., and Tawara, H., "ENERGY DEPENDENCE OF ION-INDUCED SPUTTERING YIELDS FROM MONATOMIC SOLIDS AT NORMAL INCIDENCE," *Atomic Data and Nuclear Data Tables*, Vol. 62, No. 2, 1996, pp. 149–253. https://doi.org/10.1006/adnd.1996.0005

[11] Ziegler, J. F., Ziegler, M. D., and Biersack, J. P., "SRIM – The Stopping and Range of Ions in Matter (2010)," *Nuclear Instruments and Methods in Physics Research Section B: Beam Interactions with Materials and Atoms*, Vol. 268, No. 11, 2010, pp. 1818–1823. https://doi.org/10.1016/j.nimb.2010.02.091

[12] Tran, H., and Chew, H. B., "Surface Morphology and Carbon Structure Effects on Sputtering: Bridging Scales between Molecular Dynamics Simulations and Experiments," *Carbon*, Vol. 205, 2023, pp. 180–193. https://doi.org/10.1016/j.carbon.2023.01.015

[13] Tran, H., and Chew, H. B., "Transient to Steady-State Morphology Evolution of Carbon Surfaces under Ion Bombardment: Monte Carlo Simulations," *Acta Materialia*, Vol. 263, 2024, p. 119498. https://doi.org/10.1016/j.actamat.2023.119498

[14] Nishii, K., Clark, S., Tran, H., Levin, D. A., Rovey, J., and Chew, H. B., "Carbon Sputtering and Transportation in a Ground Facility during Electric Propulsion Testing," *AIAA AVIATION 2022 Forum*, American Institute of Aeronautics and Astronautics. https://doi.org/10.2514/6.2022-3497

[15] Stuart, S. J., Tutein, A. B., and Harrison, J. A., "A Reactive Potential for Hydrocarbons with Intermolecular Interactions," *The Journal of Chemical Physics*, Vol. 112, No. 14, 2000, pp. 6472–6486. https://doi.org/10.1063/1.481208

[16] Ziegler, J. F., "The Stopping of Energetic Ions in Solids," *Nuclear Instruments and Methods*, Vol. 168, No. 1, 1980, pp. 17–24. https://doi.org/10.1016/0029-554X(80)91225-2

[17] Hakola, A., Likonen, J., Lahtinen, A., Vuoriheimo, T., Groth, M., Kumpulainen, H., Balden, M., Krieger, K., Mayer, M., Schwarz-Selinger, T., Brezinsek, S., Kelemen, M., Markelj, S., Barac, M., Gouasmia, S., Radovic, I. B., Uccello, A., Vassallo, E., Dellasega, D., Passoni, M., Sala, M., Bernard, E., Diez, M., Guillemaut, C., Tsitrone, E., Team, the A. U., Team, the Euro. M., and Contributors, the Euro. W. P., "Gross and Net Erosion Balance of Plasma-Facing Materials in Full-W Tokamaks," *Nuclear Fusion*, Vol. 61, No. 11, 2021, p. 116006. https://doi.org/10.1088/1741-4326/ac22d2

[18] Kim, S.-P., Chew, H. B., Chason, E., Shenoy, V. B., and Kim, K.-S., "Nanoscale Mechanisms of Surface Stress and Morphology Evolution in FCC Metals under Noble-Gas Ion Bombardments," *Proceedings of the Royal Society A: Mathematical, Physical and Engineering Sciences*, Vol. 468, No. 2145, 2012, pp. 2550–2573. https://doi.org/10.1098/rspa.2012.0042

[19] Harpale, A., and Chew, H. B., "Hydrogen-Plasma Patterning of Multilayer Graphene: Mechanisms and Modeling," *Carbon*, Vol. 117, 2017, pp. 82–91. https://doi.org/10.1016/j.carbon.2017.02.062

[20] Sigmund, P., "Sputtering by Ion Bombardment Theoretical Concepts," *Sputtering by Particle Bombardment I*, edited by R. Behrisch, Vol. 47, Springer Berlin Heidelberg, Berlin, Heidelberg, 1981, pp. 9–71. https://doi.org/10.1007/3540105212_7

[21] Nečas, D., and Klapetek, P., "Gwyddion: An Open-Source Software for SPM Data Analysis," *Open Physics*, Vol. 10, No. 1, 2012, pp. 181–188. https://doi.org/10.2478/s11534-011-0096-2

[22] Nixon, M. S., and Aguado, A. S., "2 - Images, Sampling and Frequency Domain Processing," *Feature Extraction and Image Processing for Computer Vision (Fourth Edition)*, edited by M. S. Nixon and A. S. Aguado, Academic Press, 2020, pp. 35–81. https://doi.org/10.1016/B978-0-12-814976-8.00002-6

[23] Bohdansky, J., "A Universal Relation for the Sputtering Yield of Monatomic Solids at Normal Ion Incidence," *Nuclear Instruments and Methods in Physics Research Section B: Beam Interactions with Materials and Atoms*, Vol. 2, No. 1, 1984, pp. 587–591. https://doi.org/10.1016/0168-583X(84)90271-4

[24] Tartz, M., "Pyrolytic Graphite and Carbon-Carbon Sputter Behaviour Under Xenon Ion Incidence," presented at the 29th International Electric Propulsion Conference, 2005.

[25] Williams, J., Johnson, M., and Williams, D., "Differential Sputtering Behavior of Pyrolytic Graphite and Carbon-Carbon Composite Under Xenon Bombardment," presented at the 40th AIAA/ASME/SAE/ASEE Joint Propulsion Conference and Exhibit, Fort Lauderdale, Florida, 2004. https://doi.org/10.2514/6.2004-3788